**Original Paper**

# Numerical Evaluation of Dynamic Transfer Matrix and Unsteady Cavitation Characteristics of an Inducer

**Koichi Yonezawa[1], Jun Aono[1], Donghyuk Kang[2], Hironori Horiguchi[1], Yutaka Kawata[3] and Yoshinobu Tsujimoto[1]**

[1]Graduate School of Engineering Science, Osaka University
1-3, Machikaneyama-cho, Toyonaka, Osaka 560-8531, Japan
yonezawa@me.es.osaka-u.ac.jp, horiguti@me.es.osaka-u.ac.jp, tujimoto@me.es.osaka-u.ac.jp,
[2] Faculty of Science and Engineering, Aoyama Gakuin University
5-10-1, Fuchinobe, Tyuo-ku, Sagamihara, Kanagawa, 252-5258, Japan
Kang@me.aoyama.ac.jp
[3] Faculty of Engineering, Osaka Institute of Technology
5-16-1 Omiya, Asahi-ku, Osaka, 535-8585, Japan
kawata@med.oit.ac.jp

## Abstract

The transfer matrix and unsteady cavitation characteristics, cavitation compliance and mass flow gain factor, of cavitating inducer were evaluated by CFD using commercial software. Quasi-steady values of cavitation compliance and mass flow gain factor were obtained first by using steady calculations at various flow rate and inlet cavitation number. Then unsteady calculations were made to determine the transfer matrix and the cavitation characteristics. The results are compared with experiments to show the validity of calculations.

**Keywords**: Inducer, dynamic transfer matrix, cavitation compliance, mass flow gain factor, CFD

## 1. Introduction

In liquid rockets, longitudinal vibration called POGO can occur through the coupling of the thrust fluctuation, structural vibration, and the fluctuation of propellant supply to the engine [1]. For the prediction of POGO instability, it is required to provide the unsteady characteristics of the feed pump represented by the transfer matrix correlating the upstream and downstream pressure and flow rate fluctuations. For non-cavitating centrifugal pumps, Ohashi has shown through theoretical study and experiments that significant delay of head development occurs above a critical frequency proportional to the rotational speed and the flow coefficient [2]. To the author's knowledge, the first introduction of transfer function as well as mass flow gain factor and cavitation compliance was made by Brennen and Acosta[3] in which they were evaluated by quasisteady calculation of blade surface cavitation. They further carried out experiments and the results are reported in [4] and [5]. Since then, several attempts [6], [7] were made to measure the unsteady cavitation characteristics. Recently, Rubin[8] re-examined the data of [4] and [5].to obtain better correlation, since the data available is limited perhaps because of the difficulty in the precise measurements of flow rate fluctuation. In addition to the use in POGO analysis, the mass flow gain factor and the cavitation compliance are important in the understanding the flow instabilities such as cavitation surge and rotating cavitation [9].

The present study is intended to evaluate the transfer function, mass flow gain factor and cavitation compliance by using CFD. The results are compared with collection of data available from recent review article by Brennen [10].

## 2. Computational methods

Calculations were made on an inducer similar to the oxygen Turbopump of LE-7 for H-II rocket, using a commercial code ANSYS-CFX12.0. The geometry and the specifications of the inducer are shown in Fig. 1 and Table 1. The $k$-$\omega$ turbulence model was used. The cavitation model is based on the homogeneous multiphase flow solver taking account of the dynamics of cavitation bubble by solving the simplified Rayleigh-Plesset equation [11]. This effect is taken into account by adding a special source term into the continuity equation. It is assumed that the vapor bubbles are moving without slip and the velocity fields for all phases are the same.
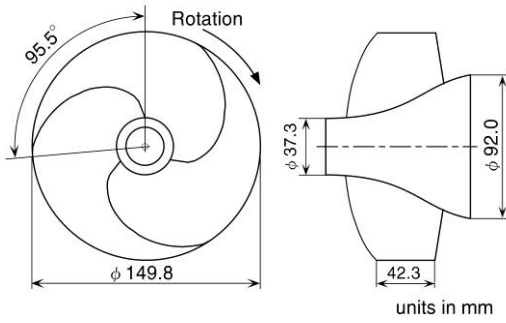
**Fig. 1** Inducer geometry

**Table 1** Principal dimensions of test inducer

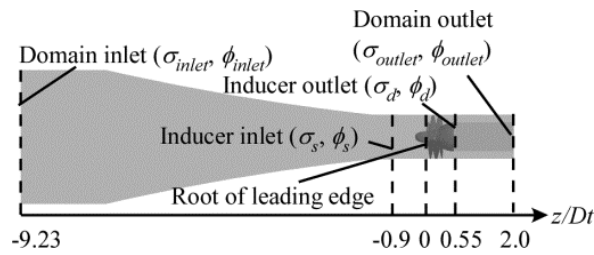| | |
|---|---|
| Number of blades | 3 |
| Tip diamter, $D_t$ | 149.8mm |
| Inlet tip blade angle | 7.5° |
| Outlet tip blade angle | 9.0° |
| Hub/tip ratio at inlet | 0.25 |
| Hub/tip ratio at outlet | 0.51 |
| Solidity at tip | 1.91 |
| Design flow coefficient, $\phi_{design}$ | 0.078 |



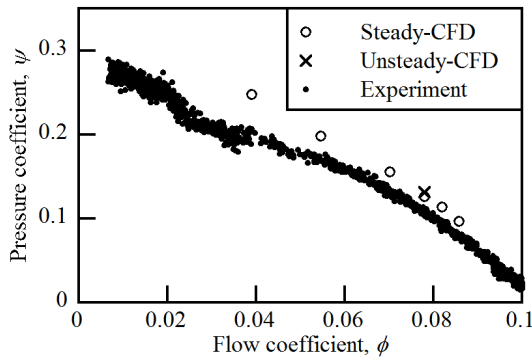**Fig. 2** Computational domain for unsteady flow calculation



**Fig. 3** Performance curve under non-cavitating condition
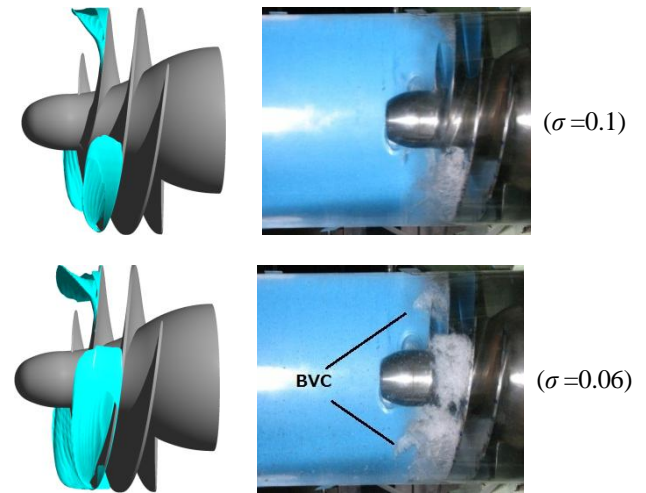


**Fig. 4** Geometries of cavity (left: iso-void fraction surface at 0.01 by numerical simulation, right: experimental snapshot, BVC: Backflow vortex cavitation )

Figure 2 shows the computational domain for unsteady calculations. The nozzle type inlet pipe is used for better stability of numerical calculations. For steady calculations, a cylindrical inlet pipe with the length of $5.4D_t$ and the downstream cylindrical casing and the hub with the length of $5.15\ D_t$ has been used. To minimize the computational time, calculations were made on one pitch assuming the pitchwise periodicity. For steady calculations, the total pressure was specified at the inlet of the domain and the mass flow at the outlet. Two types of unsteady calculations were made to determine the transfer matrix. In one of them, the flow rate is specified at the inlet of the domain and the static pressure at the outlet. In the other, the flow rate is specified at the outlet and the pressure at the inlet. The total number of mesh for unsteady calculations is 653,107 with 557,207 allocated near the inducer, and 2,280,737 total number of meshes were used for steady calculations with 1,754,133 meshes near the inducer . The mesh size and the typical time step 1/2000 of revolution was determined so that the continuity equation $dV/dt = Q_2 - Q_1$, where $V$ is the cavity volume evaluated from the integration of void fraction and $Q_1$ and $Q_2$ are inlet and outlet flow rate, is satisfied with acceptable level. The unsteady calculations were continued until similar results are obtained over three cycles of oscillation. It took 2-3 weeks by a personal computer for one case of unsteady computations.
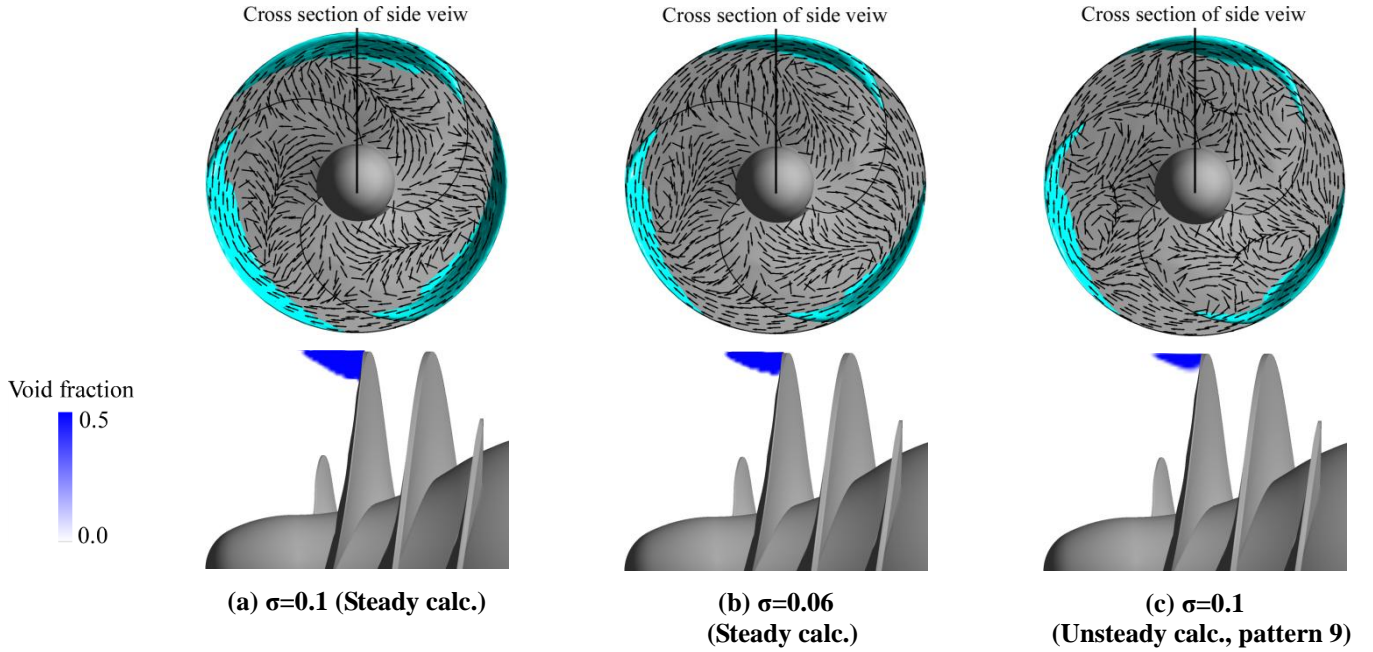
**(a) σ=0.1 (Steady calc.)**  **(b) σ=0.06 (Steady calc.)**  **(c) σ=0.1 (Unsteady calc., pattern 9)**

**Fig. 5** Front and side views of cavities and the velocity vector at $z=0$
(top: front view and velocity vector, bottom: side view)

The non-cavitating pressure coefficient $\psi=(p_d - p_s)/(0.5\rho U_t^2)$ based on the inlet and outlet pressure $p_s$, $p_d$ and the tip speed $Ut$ is compared with experiments (small dots) in Fig. 3, where $\phi=C_z/U_t=Q/A_i U_t$ is the flow coefficient based on the mean axial velocity $C_z$, at $z=0$. The closed type cavitation tunnel was used for measurement [12]. The difference between the predictions using the steady and the unsteady calculations is small.

In Fig. 4, the cavity geometry at the design flow coefficient $\phi_{design}=0.078$ is compared with that from steady calculation shown by the surface with the void fraction $\alpha=0.01$. Backflow vortex cavitations are found in the experiment at the cavitation number $\sigma\equiv(p_s - p_v)/(0.5\rho U_t^2)=0.06$ where $p_v$ is the saturated vapor pressure. This could not be simulated by the steady calculation.

## 3. Steady calculations and quasi-steady evaluation of cavitation compliance and mass flow gain factor

Steady calculations were made to evaluate the cavitation compliance $K$ and mass flow gain factor $M$ defined as

$$K \equiv -\partial V^*/\partial \sigma \tag{1}$$
$$M \equiv -\partial V^*/\partial \phi \tag{2}$$

where $V^*=V/(HA_i)$ is the cavity volume normalized with the blade spacing $H=\pi D_t/3$ at the tip and the cross sectional area $A_i$ at $z=0$.

The front and side views of cavities and the absolute velocity vector at $z=0$ are shown in Fig. 5 at the design flow coefficient $\phi_{design}=0.078$. The cavity occurs only near the tip, without blade surface nor backflow vortex cavitation. With steady calculation, we can observe a tangential flow region near the casing. This tangential flow is caused by the backflow from the impeller. The shear layer between the swirling backflow and the main flow rolls up and forms a backflow vortex structure. We can observe three vortices and six vortices in results of steady and unsteady calculations, respectively. The backflow vortex structure rotates at the speed of $0.16U_t$ for the unsteady calculation result. The backflow vortices are visualized by cavitation in the picture shown in Fig. 4 at $\sigma=0.06$ but not at $\sigma=0.10$. So, the steady calculation at smaller cavitation number fails to take account of the backflow vortex cavitation. However, the effects of the backflow vortex cavitation can be neglected at least at $\sigma=0.10$.

Figure 6 (a) shows the plot of the non-dimensional cavity volume evaluated from the integration of void fraction from steady calculations. The values of cavitation compliance and mass flow gain factor are obtained from the finite difference approximation of Eq.(1) and (2) and shown in Fig. 6 (b) and (c). Although we observe a general tendency that both cavitation compliance and mass flow gain factor are larger at smaller cavitation number and smaller flow rate, there exists some violation from this tendency.

The values at the design flow coefficient are re-plotted on the recent data set prepared by Brennen [10] in Fig. 7. Although the value of cavitation compliance agrees with other data, the present calculation gives significantly smaller value of mass flow gain factor.

## 4. Unsteady calculations and dynamic transfer matrix

We assume that the fluctuating part of the normalized inlet (suffix $s$) and outlet (suffix $d$) pressure and flow coefficients $\tilde{\sigma}_{s,d} \equiv \tilde{p}_{s,d}/(0.5U_t^2)$, and $\tilde{\phi}_{s,d}$ are much smaller than the mean part and correlate them by using a transfer matrix $[T_{i,j}]$ as follows [3]:
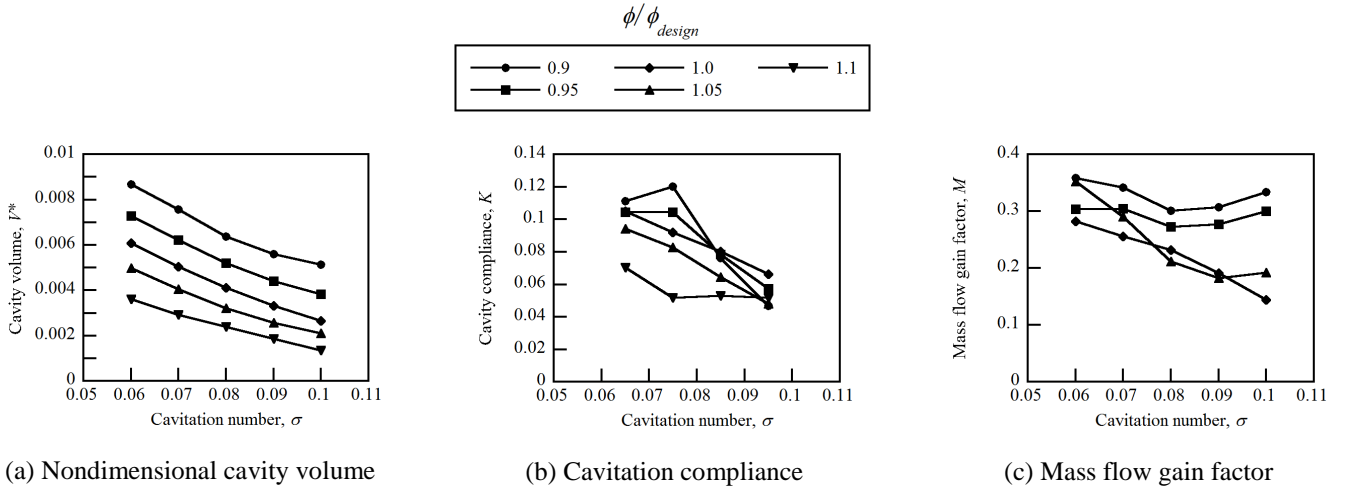
(a) Nondimensional cavity volume     (b) Cavitation compliance     (c) Mass flow gain factor

**Fig. 6** Cavity volume (a), cavitation compliance (b) and mass flow gain factor (c) estimated from steady calculations ($\sigma$=0.1).
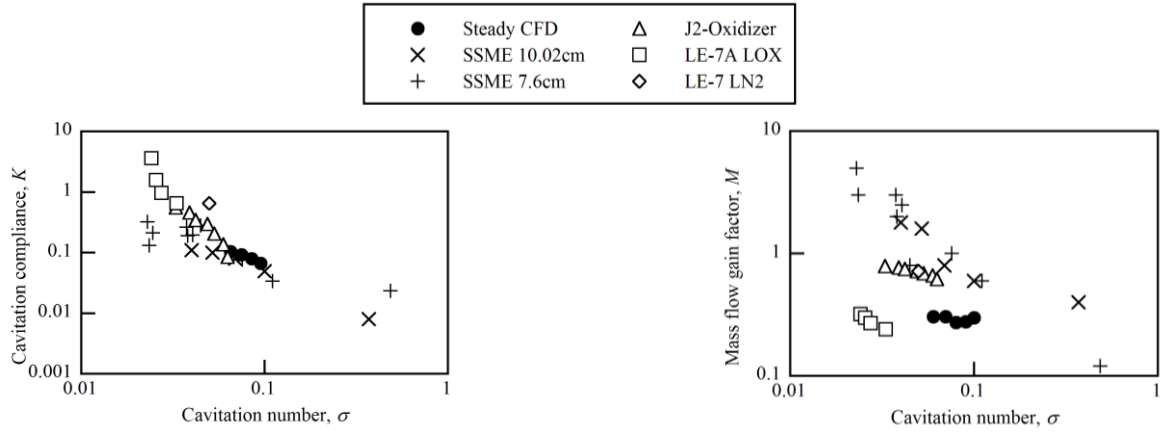


**Fig. 7** Comparison of cavitation compliance (left) and mass flow gain factor (right) between the present results ($\phi$=0.078) and various experimental data [5].

$$\begin{pmatrix} \tilde{\sigma}_d \\ \tilde{\phi}_d \end{pmatrix} = \begin{bmatrix} T_{11} & T_{12} \\ T_{21} & T_{22} \end{bmatrix} \begin{pmatrix} \tilde{\sigma}_s \\ \tilde{\phi}_s \end{pmatrix} \tag{3}$$

We assume all the elements in Eq.(3) fluctuates with the time dependence of $e^{j\omega\tau}$ with the non-dimensional angular frequency $\omega=2\pi f H/U_t$, the dimensional frequency $f$, dimensional and non-dimensional time $t$ and $\tau=t/(H/U_t)$, and the imaginary unit $j$. Then, the definitions of cavitation compliance and mass flow gain factor, Eqs.(1) and (2), and the continuity equation results in

$$dV*/d\tau = \tilde{\phi}_d - \tilde{\phi}_s = -j\omega K \tilde{\sigma}_s - j\omega M \tilde{\phi}_s \tag{4}$$

By using the resistance and the inertance of the flow elements upstream and downstream of the cavitating region by $R_{s,d}$ and $L_{s,d}$, we can represent

$$\tilde{\sigma}_d - \tilde{\sigma}_s = -(R_d + j\omega L_d)\tilde{\phi}_d - (R_s + j\omega L_s)\tilde{\phi}_s \tag{5}$$

From Eqs.(4) and (5), we can express the transfer function as follows:

$$\begin{bmatrix} T_{i,j} \end{bmatrix} = \begin{bmatrix} 1 + j\omega K R_d - \omega^2 L_d K, & (-R_d - j\omega L_d)(1 - j\omega M) - (-R_s - j\omega L_s) \\ -j\omega K, & 1 - j\omega M \end{bmatrix} \tag{6}$$

Here, our purpose is to determine the values of four elements of $\begin{bmatrix} T_{i,j} \end{bmatrix}$ from unsteady calculations. Since we can obtain two relations correlating the upstream and downstream pressure and flow rate fluctuations from the calculation of one case, we need two independent cases of calculations with the same excitation frequency. For this purpose, we specified the flow rate fluctuation at the inlet boundary of the domain in one case, and at the outlet in another case. The pressure was specified on the boundary where the boundary conditions of flow rate is not specified. To confirm the validity, another method was examined for some cases. In this method,

**Table 2** Computational conditions

| Pattern | Excitation frequency, $\omega h/U_t$ | Excitation amplitude, $\tilde{\phi}_{s,d}/\bar{\phi}$ (%) | Inducer rotational Speed,$\Omega$ [rpm] | Domain type | Flow rate given at | Time step(sec) | Inlet cavitation number, $\sigma_s$ |
|---|---|---|---|---|---|---|---|
| 1 | 0.168 | 0.75 | 1500 | domain1 | downstream | $1.0\times10^{-4}$ | 0.094 |
| 2 | 0.168 | 0.75 | 1500 | domain1 | upstream | $1.0\times10^{-4}$ | 0.101 |
| 3 | 0.251 | 1 | 1500 | domain1 | downstream | $5.0\times10^{-5}$ | 0.094 |
| 4 | 0.251 | 1 | 1500 | domain1 | upstream | $5.0\times10^{-5}$ | 0.101 |
| 5 | 0.524 | 2 | 3000 | domain1 | downstream | $1.0\times10^{-5}$ | 0.094 |
| 6 | 0.524 | 0.75 | 3000 | domain1 | upstream | $1.0\times10^{-5}$ | 0.101 |
| 7 | 0.524 | 2 | 3000 | domain2 | downstream | $1.0\times10^{-5}$ | 0.094 |
| 8 | 0.838 | 2 | 3000 | domain1 | downstream | $1.0\times10^{-5}$ | 0.095 |
| 9 | 0.838 | 0.75 | 3000 | domain1 | upstream | $1.0\times10^{-5}$ | 0.101 |
| 10 | 0.838 | 0.5 | 3000 | domain2 | downstream | $1.0\times10^{-5}$ | 0.094 |

(a) pattern 1
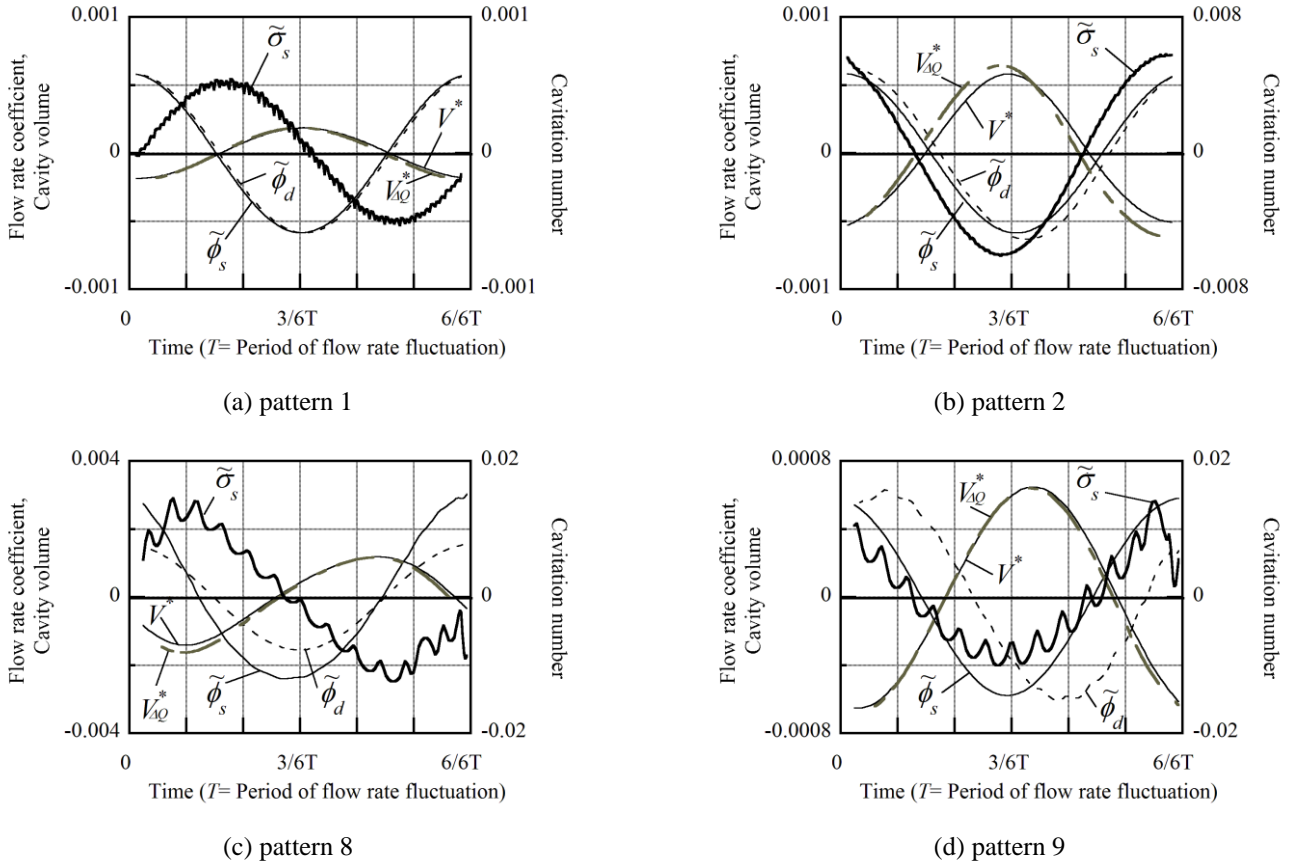
(b) pattern 2

(c) pattern 8

(d) pattern 9

**Fig. 8** Time histories of flow coefficient, pressure coefficient and cavity volume fluctuations during one cycle of flow rate fluctuation.

calculations were made with the domain (domain1) shown in Fig. 2 and another domain (domain 2) with the inlet pipe extended by $14D_t$, with specifying the flow rate at the outlet and the pressure at the inlet, for both cases. The conditions for the calculations are summarized in Table.2. Unsteady calculations were made only at the design flow coefficient of $\phi_{design}$=0.078 and the cavitation number of $\sigma$ =0.1. The rotational speed was determined to match the experiments being carried out in parallel with the present calculations.

Some examples of oscillations of upstream and downstream flow coefficients, pressure coefficient at the inlet, and the cavity volume oscillations are shown in Fig. 8. The cavity volume was evaluated by two methods: from the integration of void fraction $\tilde{V}*$ and from the difference of the upstream and downstream flow rates, $\tilde{V}*_{\Delta Q}$. Better agreements would be obtained by using finer mesh and smaller time step. In the cases of flow rate specification at the outlet (Pattern 1 and Pattern 8), the phase of the inlet pressure and flow rate fluctuations differs about $\pi/2$. On the other hand, the phase is nearly the same for the cases of inlet excitation (Pattern 2 and Pattern 9), showing that "independent" excitation mode was obtained. The higher frequency oscillation of the inlet pressure is caused by the interaction of blades with the inlet vortex structure shown in Fig. 5 [13].

Fig. 9 shows the relative velocity vector and the void fraction in the cylindrical planes with $r/R_t$=0.93 and 0.99 for the case of Pattern 9. For this case, the inlet flow coefficient and the pressure becomes minimum at 3/6T as shown in Fig. 8 (d). The size of the cavity shown by the void fraction becomes the maximum at 4/6T, suggesting significant delay of cavity response, although the delay of total cavity volume from the integration of void fraction is much smaller. The velocity vectors show that the flow gets into/out from the cavitating region, typical for bubbly flow cavitation.
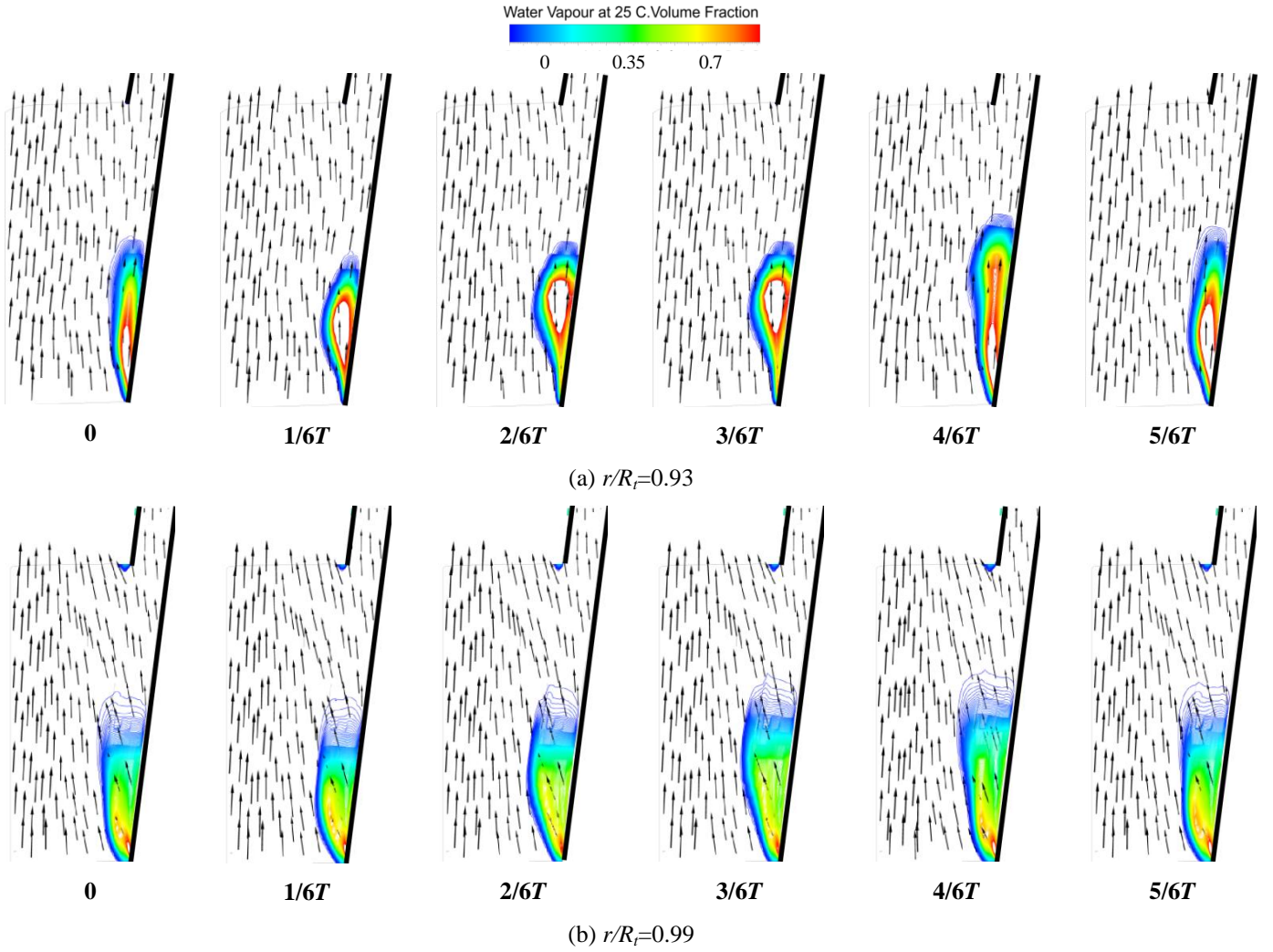
Water Vapour at 25 C.Volume Fraction

0    0.35    0.7

| 0 | 1/6*T* | 2/6*T* | 3/6*T* | 4/6*T* | 5/6*T* |

(a) $r/R_t$=0.93

| 0 | 1/6*T* | 2/6*T* | 3/6*T* | 4/6*T* | 5/6*T* |

(b) $r/R_t$=0.99

**Fig. 9** Void fraction distribution and relative velocity vector in cylindrical plane (Pattern 9)

Figure 10 compares the transfer matrix elements obtained in the present calculations with the original experimental results by Brennen [5] and the correlation given by Rubin[8] based on the same experimental data. Open symbols show the results based on the calculations on the same domain geometry shown in Fig. 2, and the closed symbols using the results with extended inlet pipe (from Pattern 5,7 and 8,10). We observe small differences suggesting that the methods applied are both acceptable. The results in [5] and [8] are based on total pressure, although the present study is based on static pressure. To see the difference, the transfer matrix elements were calculated also on the total pressure basis and the results are shown by + for $\omega$=0.838. The difference is negligible.

As to $T_{11}$, the results show that the dependence of on $\omega$ suggested by Eq.(6) is adequate, although the effect of $\omega$ looks to be smaller than the experimental results. In the plot of $T_{12}$, the quasi-steady resistance $-R_d=d\psi/d\phi$ evaluated from the slope of the performance curve in Fig.3 is shown in the figure. The difference of the real part from this value is small even at higher frequency. The inertance $L_d+L_s$ is evaluated from the total axial length of the region without the blade between inlet and outlet plus the blade length at the tip. The effect of inertance thus evaluated is also shown in the figure. The absolute value of the imaginary part is somewhat larger than the simple evaluation. The real part of $T_{21}$ have small values although Eq.(6) suggest that it should be zero if the cavitation compliance $K$ is real. Imaginary part is proportional to the frequency as suggested by Eq.(6). The real part of $T_{22}$ decrease from the value of 1 and the imaginary part has a small negative value. In all cases, the results obtained from the present calculations agree with the experimental results at least qualitatively.

Unsteady cavitation compliance and mass flow gain factor are determined from

$$K = T_{21} j / \omega \qquad (7)$$
$$M = (T_{22} - 1) j / \omega \qquad (8)$$

and shown in Fig. 11. The results from the cavity volume from the integration of the void fraction and that from the flow rate difference are compared. Although we do have some difference, general tendencies can be discussed. The figure also shows the results of steady calculations with finer mesh. The unsteady results approximately tends to the quasisteady values in the limit of $\omega\rightarrow0$. The results obtained by applying Eq. (7) and (8) on Rubin's correlations of $T_{ij}$ based on Brennen's experimental data are also shown. These results and the definitions of $M$ and $K$ given by Eq.(1) and (2) show that the cavity volume responds to the flow rate and inlet pressure fluctuations with some delay, as typically shown in Fig. 9.
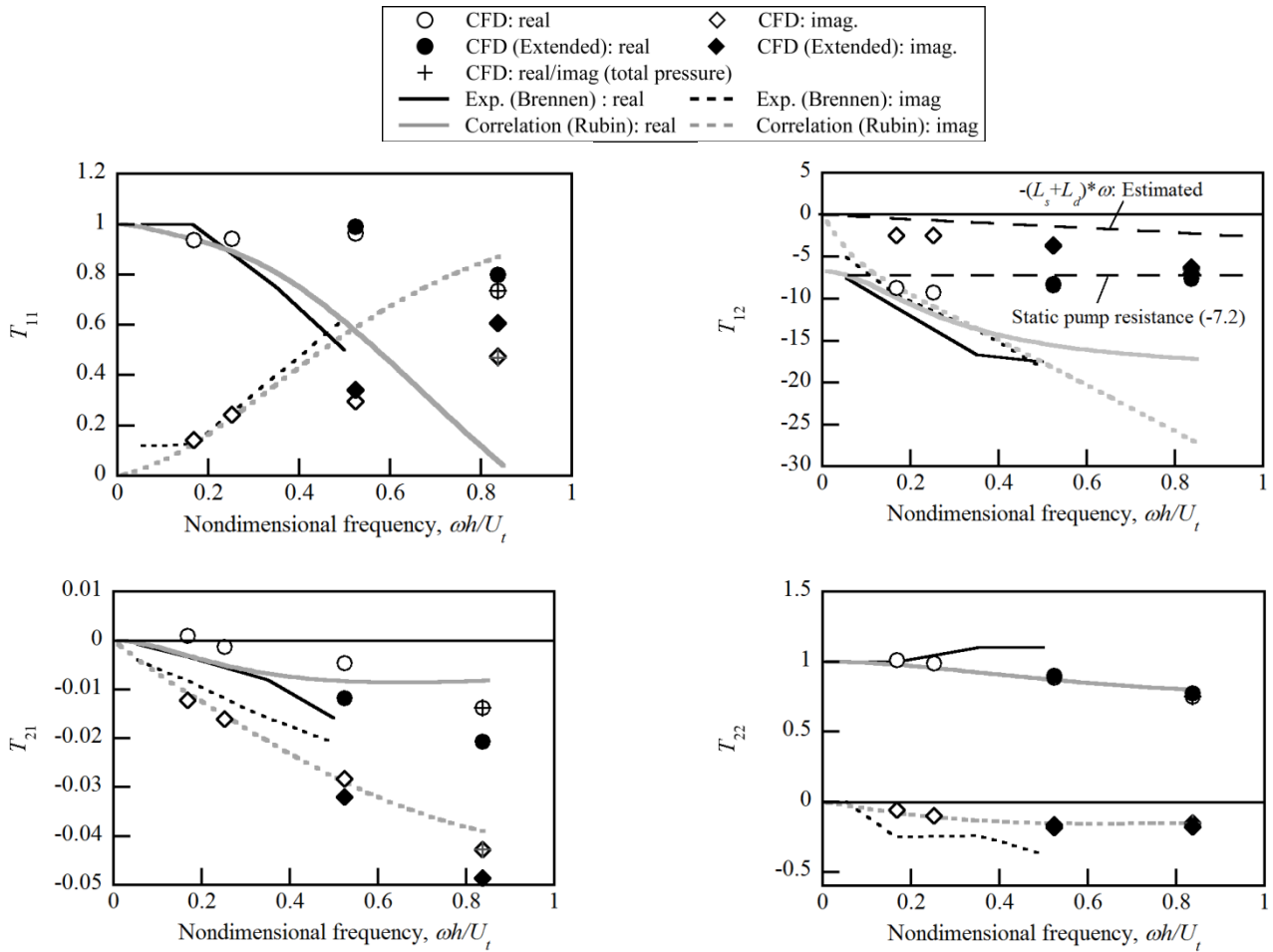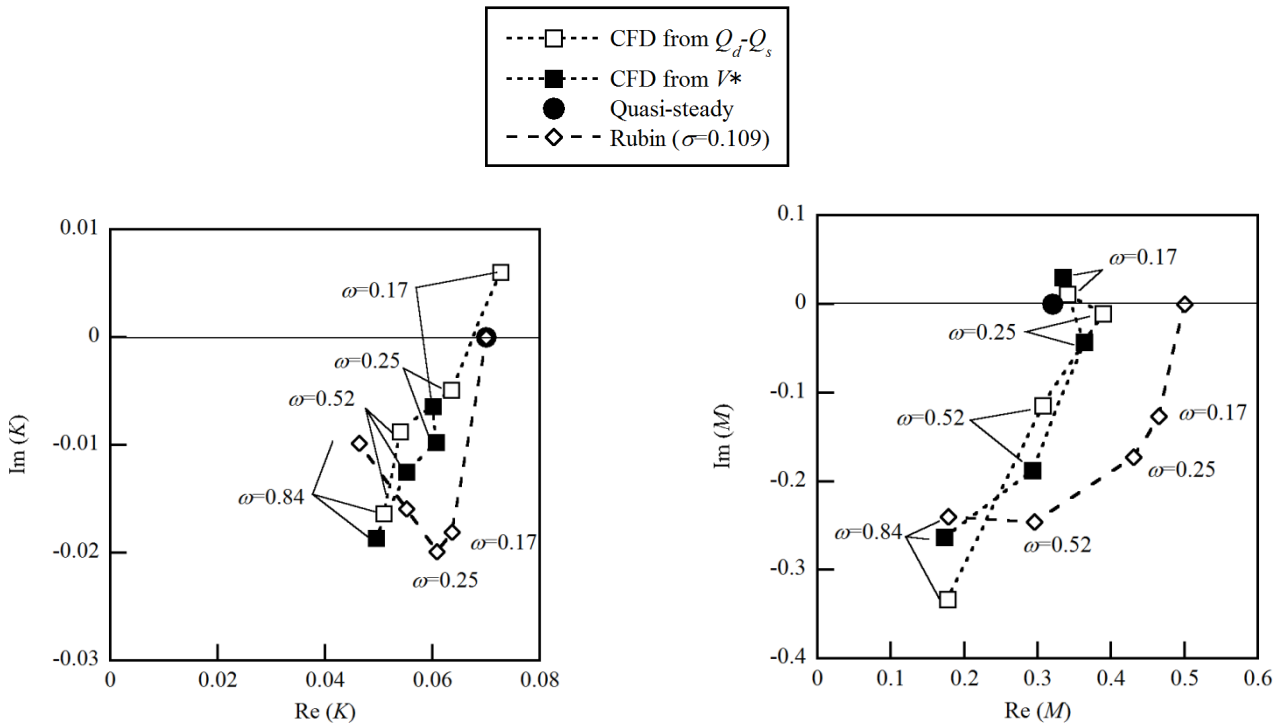
**Fig. 10** Transfer matrix elements at $\sigma=0.1$.



**Fig. 11** Unsteady cavitation compliance and mass flow gain factor at $\sigma=0.1$.

## 5. Concluding remarks

It has been shown that it is now possible to evaluate the unsteady cavity response and the dynamic transfer functions by careful application of a commercial code, at least qualitatively. The results are compared with experimental results obtained in 1982 and they agree reasonably. The CFD was applied only to higher cavitation number at design flow rate, where the blade surface cavitation and backflow vortex cavitation is unimportant. We should extend the present method to cover the case of smaller cavitation number to clarify the contributions of tip cavitation, blade surface cavitation and backflow vortex cavitation. Cavitation instabilities such as rotating cavitation and alternate blade cavitation could be explained by the interaction of local flow near the cavity closure with the next blade [13]. We need to bridge the understanding from the local flow with the global view based on mass flow gain factor and cavitation compliance.

Systematic experiments to measure the unsteady cavitation characteristics are still rare. The authors are now conducting such experiments but still have some problems. We are hoping to make more quantitative comparisons with experiments in the near future.

## Acknowledgments

## Nomenclature

| | | | | |
|---|---|---|---|---|
| $\alpha$ | Void fraction | | $T_{ij}$ | Transfer matrix |
| $D_t$ | Inducer tip diameter | | $U_t$ | Tip speed |
| $f$ | Frequency | | $V$ | Cavity volume |
| $\phi$ | Flow coefficient | | $\omega$ | Angular frequency |
| $H$ | Blade spacing | | $\psi$ | Pressure coefficient |
| $K$ | Cavitation compliance | | $z$ | Axial coodinate |
| $L$ | Inertance | | Suffix | |
| $M$ | Mass flow gain factor | | 1 | Inlet value |
| $p$ | Pressure | | 2 | Outlet value |
| $Q$ | Flow rate | | $s$ | Upstream value |
| $R$ | Resistance | | $d$ | Downstream value |
| $\sigma$ | Cavitation number | | $design$ | Design value |

## References

[1] Rubin, S., 1966, "Longitudinal Instability of Liquid Rockets Due to Propulsion Feedback (POGO)," Journal of Spacecraft, Vol. 3, No. 8, pp. 1188-1195.

[2] Ohashi, H., 1968, "Analytical and Experimental study of Dynamic Characteristics of Turbopumps," NASA TN D-4298, pp. 1-109.

[3] Brennen, C. and Acosta, A., 1976, "The Dynamic Transfer Function for a Cavitating Inducer," Journal of Fluid Engineering, Vol. 98, pp. 182-191.

[4] Ng, S. L. and Brennen, C., 1978, "Experiments on the Dynamic Behavior of Cavitating Pumps," Journal of Fluids Engineering, Vol. 100, pp. 166-176.

[5] Brennen, C. E., Meissner C., Lo, E. Y., Hoffman, G. S., "Scale Effects in the Dynamic Transfer Functions for Cavitating Inducers," Journal of Fluids Engineering, Vol. 104, pp. 428-433.

[6] Shimura, T., 1995, "Geometry-Effects in the Dynamic Response of Cavitating LE-7 Liquid-Oxygen Pump," AIAA Journal of Propulsion and Power, 11, No. 2, 330-336.

[7] Iacopozzi, M., Lignaporo, V. and Prevel, D., 1993, "POGO Characteristics of ARIANE V Turbopump LOX Pump with Hot Water," AIAA Paper 93-2124.

[8] Rubin, S., 2004, "An Interpretation of Transfer Function Data for a Cavitating Pump," AIAA Paper 2004-4025.

[9] Tsujimoto, Y., Kamijo, K. and Brennen, C. E., 2001, "Unified Treatment of Instabilities of Turbomachines," Journal of Propulsion and Power, Vol. 17, No. 3, (2001-3-9), pp. 636-643.

[10] Brennen, C.E., 2012, "A Review of the Dynamics of Cavitating Pump," to be presented at the 26th IAHR Symposium on Hydraulic Machinery and Systems, Beijing, China.

[11] Bakir, F., Rey, R., Gerber, A.G., Belamri, T. and Hutchinson, B., 2004, "Numerical and Experimental Investigations of the Cavitating Behavior of an Inducer," Internationla Journal of Rotating Machinery, Vol. 10, Issue 1, pp. 15-25.

[12] Kang, D., Watanabe, T., Yonezawa, K., Horiguchi, H., Kawata, Y. and Tsujimoto, Y., 2009, "Inducer Design to Avoid Cavitation Instabilities," International Journal of Fluid Machinery and Systems, Vol. 2, No. 4, (2009-10), pp. 439-448.

[13] Kang, D., Yonezawa, K., Horiguchi, H., Kawata, Y. and Tsujimoto, Y., 2009, "Cause of Cavitation Instabilities in Three-Dimensional Inducer," International Journal of Fluid Machinery and Systems, Vol. 2, No. 3, (2009-9), pp. 206-214.